




Weiyu Liu¹
 Yukun Ren^{2,3} 
 Feng Chen^{1*}
 Jingni Song¹
 Ye Tao²
 Kai Du¹
 Qisheng Wu¹

¹School of Electronics and Control Engineering, School of Highway, Chang'an University, Xi'an, Shaanxi, P. R. China

²State Key Laboratory of Robotics and System, Harbin Institute of Technology, Harbin, Heilongjiang, P. R. China

³The State Key Laboratory of Nonlinear Mechanics (LNM), Chinese Academy of Sciences, Institute of Mechanics, Beijing, P. R. China

Received November 9, 2018

Revised March 12, 2019

Accepted March 14, 2019

Research Article

A microscopic physical description of electrothermal-induced flow for control of ion current transport in microfluidics interfacing nanofluidics

The phenomenon of electrothermal (ET) convection has recently captured great attention for transporting fluidic samples in microchannels embedding simple electrode structures. In the classical model of ET-induced flow, a conductivity gradient of buffer medium is supposed to arise from temperature-dependent electrophoretic mobility of ionic species under uniform salt concentrations, so it may not work well in the presence of evident concentration perturbation within the background electrolyte. To solve this problem, we develop herein a microscopic physical description of ET streaming by fully coupling a set of Poisson-Nernst-Planck-Navier-Stokes equations and temperature-dependent fluid physicochemical properties. A comparative study on a standard electrokinetic micropump exploiting asymmetric electrode arrays indicates that, our microscopic model always predicts a lower ET pump flow rate than the classical macroscopic model even with trivial temperature elevation in the liquid. Considering a continuity of total current density in liquids of inhomogeneous polarizability, a moderate degree of fluctuation in ion concentrations on top of the electrode array is enough to exert a significant influence on the induction of free ionic charges, rendering the enhanced numerical treatment much closer to realistic experimental measurement. Then, by placing a pair of thin-film resistive heaters on the bottom of an anodic channel interfacing a cation-exchange medium, we further provide a vivid demonstration of the enhanced model's feasibility in accurately resolving the combined Coulomb force due to the coexistence of an extended space charge layer and smeared interfacial polarizations in an externally-imposed temperature gradient, while this is impossible with conventional linear approximation. This leads to a reliable method to achieve a flexible regulation on spatial-temporal evolution of ion-depletion layer by electroconvective mixing. These results provide useful insights into ET-based flexible control of micro/nanoscale solid entities in modern micro-total-analytical systems.

Keywords:

Electrothermal convection / Ion transport control / Micro/nanofluidics / Salt concentration perturbation / Smeared interfacial polarization

DOI 10.1002/elps.201900105

Correspondence: Dr. Yukun Ren, State Key Laboratory of Robotics and System, Harbin Institute of Technology, West Da-Zhi Street 92, Harbin, Heilongjiang, P. R. China

Fax: +86-0451-86402658

E-mail: rykhit@hit.edu.cn

Abbreviations: **B.C.**, boundary condition; **DBL**, diffuse boundary layer; **DEP**, dielectrophoresis; **EHD**, electrohydrodynamic; **EI**, electroconvective instability; **EO**, electroosmosis; **EPM**, electrophoretic mobility; **ESCL**, extended space charge layer; **ET**, electrothermal; **ICEO**, induced-charge electroosmosis; **ICP**, ion concentration polarization; **IDL**, induced double layer; **IDZ**, ion-depletion zone; **NC**, natural convection

1 Introduction

Lab-on-a-chip technologies require the development of new techniques for manipulation of fluids at the nanoliter scale [1, 2]. Discrete electrodes embedded in microchannels indicate a potential opportunity for electrokinetic actuation either on the liquid medium or on granular samples suspended in the buffer solution [3]. Electrohydrodynamics (EHDs) has been acquiring unprecedentedly increasing attention from the microfluidic community since the last two decades [4–6]. Traditional DC electroosmosis (EO) [7, 8], electrowetting on dielectrics [9], injection EHD [10], conduction

*Additional corresponding author: Professor Feng Chen
Email: chenfeng@chd.edu.cn

Color online: See the article online to view Figs. 1–9 in color.

EHD [11], traveling-wave induction EHD [12–15], induced-charge electroosmosis (ICEO) [16–24], dielectrophoresis (DEP) [25–30], electrothermal (ET) induced flow [31–37], and electroconvective instability (EI) [38–40] near a permselective membrane are all authoritative methodologies where electric fields are employed to actuate liquid solutions in miniaturization systems.

The fast development of micro-machining technology in the last 10 years has allowed for an ease with which microelectrode structures can be patterned and then integrated into microfabricated fluidic networks. For such, both steady and alternating electric fields as well as hybrid DC/AC voltage signals have been broadly employed to deal with particle and liquid contents in microfluidics [41–48].

Unlike EO, ICEO and EI, all of which have close bearing with the mechanism of Debye screening, DEP and ET are originated by structural polarization for inhomogeneous materials. Particle DEP has a surface-coupled nature, in that electrical properties are piecewise constant on either side of the phase boundary. By contrast, the academical term ‘smeared structural polarizations’ was recently proposed by Gimsa et al. to reveal the physical essence of ACET [31, 49, 50]. This phrase vividly describes the dispersive feature of solution conductivity under non-uniform heating for ET, in which an externally-imposed electric field acts on its own induced charge for engendering steady convection of saline solution. Given its docile nature and ease of implementation with simple electrode structures, ET has been widely applied in microfluidics for various important applications, especially in cases that demand actuation of high-conductivity biological fluids. Kunti and co-researchers have recently conducted a series of theoretical investigations on ET actuation of the phase interface between immiscible binary flows [5, 6, 51]. In their great work, time-averaged ACET vortex flow motion in the bulk and nonlinear Maxwell electrical stress at the sharp material interface in externally-imposed AC/DC fields are combined delicately for propelling the insulating liquid phase in direct contact with electrolyte solution [52, 53]. These pioneering researches provide a solid foundation for active control of two-phase flow using ET effect in practical experiments. The classical model of ET from Ramos et al. was derived under the approximation of small gradients of temperature [3], and more importantly, it has been found that the variation in liquid conductivity with temperature occurs due to a change in electrophoretic mobility (EPM) [54]. That is, it has arbitrarily excluded the possibility of fluctuation in salt concentration across the thin liquid layer. However, gradient in ion number density may appear as either concentration polarization or in the form of an externally-imposed conductivity gradient.

By taking strong thermal-electric coupling and a more exact body force density into account, two recent theoretical and experimental studies on characterization of ET flow have in coincidence developed an identical physical model from the macroscopic perspective [12, 55]. This special numerical treatment predicts a larger flow rate than the classical model. The reason behind is that an increase in ion mobility with temperature elevation will in turn raise the temperature in

electrolyte solution by the same amount. Nevertheless, it disregards the effect that perturbation of ion concentration has on the conservation of electric current density as well, and thereby still cannot explain why the measurement data of ET pump flow rate are lower than that predicted by numerical simulation [56].

To address this issue, we establish herein a unique microscopic physical description of ET convection. Our enhanced model directly accounts for mass conservation of ionic charge carriers in electrolyte, which possesses inhomogeneous material properties due to non-uniform heating. Correlating salt concentration with volumetric free charge density through Gauss law, our model successfully resolves the hitherto unexplained theoretical overestimation of ET flow rate. It is discovered that a subtle decrease in ion concentration is observable on top of the electrode gap of a maximum temperature rise in the framework of a standard ACET micropump (case 1), implying that great advances are going to be made in the theoretical formulation of ET effects.

However, this is still not enough to demonstrate the feasibility of this enhanced treatment in accurately resolving the fluid physics of ET, when either strong ion concentration perturbation occurs or some other electrodynamic effects coexist in similar device design. The group of Yossifon has recently demonstrated that an ion depletion layer’s length in the anodic microchannel adjacent to an ion-permselective membrane can be dynamically controlled by producing controlled ET vortices [57], which are driven by the strong interaction of temperature gradients with an externally-imposed current source. In this occasion, the occurrence of ion concentration polarization (ICP) serves as a natural origin of strong perturbation of background ion number density [58]. Besides, EO and natural convection (NC) may interfere with ET vortex flow field in this special micro/nanofluidic device. Inspired by this great work (case 2), we attempt to make use of the enhanced model to test its feasibility in resolving accurately the transient distribution of induced space charge density and the charge carriers’ concentration field under the influence of complicated fluid dynamics. As expected from the simulation result, when the depleted wavefront propagates forward, strong ET convection emerges as long as the local field strength at the position of the temperature maximum becomes sufficiently large. Only when the diffuse boundary layer (DBL) passes over the top of a series of microheaters embedded at the channel bottom surface, a combined action of ET and NC inhibits efficiently the dynamic growth of ion-depletion zone (IDZ). This implies our model is able to capture the spatial-temporal evolution of DBL’s growth under electroconvective mixing more accurately, as compared to the classical linear approach. Such active control of ion transport based on ET whirlpools can find broad applications in enhancing on-chip electro dialysis by inducing thinner ion-depletion layers, lowering the microchannel resistance for biosensing in nanoscale ducts, and regulating the location of preconcentrated plug of charged analytes. By studying the second situation, we proved that this enhanced treatment is able to resolve accurately the fluid physics of ET, even in the presence of strong ICP and other

coexisting electrodynamic effects. Accordingly, our work makes substantial contributions to the field of electrokinetic micro/nanofluidics, in terms of presenting a unique microscopic interpretation of ET streaming, which is even valid under intense background salt concentration perturbation affected by various fluid transport phenomena.

2 Methods

2.1 Model geometry

Our simulation analysis focused on two device designs for distinct purposes. The first one is a standard electrokinetic fluidic pump, where an asymmetric microelectrode array is embedded at the bottom of a straight main channel full of saline solution (Fig. 1A and B). Application of an AC voltage signal of $V_{AC} = V_0 \cos(\omega t)$ to the driving electrode pair can actuate steady transport of aqueous electrolyte via ET mechanism, which would pump unidirectionally from the narrower electrode to the wider counterpart on top of the ideally polarizable surfaces, as long as there is discernable temperature gradient across the thin liquid layer of H in thickness. The width of the two adjacent metal strips is W_1 and W_2 for the narrower and wider one, respectively, with the nearest gap size between them being W_{G1} . The distance between one pairwise in two neighboring units is W_{G1} , so the characteristic repeating wavelength for such pump structure is given by $\lambda = W_1 + W_2 + W_{G1} + W_{G2}$. This device model is aimed for validation of the improved physical interpretation developed herein, which considers current continuity of charge carriers' motion in the context of mass conservation at the microscopic level. Since the dimension along the length of electrode bars can be made infinitely long in reality, it is appropriate for us to ignore any out-of-plane effect and conduct this comparison investigation using 2D representation, which contains the major path via which the flow is transported across the main channel.

The second scenario involves a micro/nanofluidic hybrid system (Fig. 1C and D), in which two microchambers sandwich a central ion-permselective medium. When imposing a constant current source across the farthest ends of the fluidic system, an electric current of a fixed magnitude $I = I_{app}$ can be maintained across the nanoporous membrane, which passes from the anodic to the cathodic chamber via electrophoretic transport of ionic species. The ability to induce ion enrichment at the cathodic chamber and ion depletion at the anodic chamber interfacing a cation-selective medium, a phenomenon called ICP, has been well studied for such device design. However, the length of depletion zone is routinely determined by fixed geometry and material properties of the nanochannel that are key to the device functionality, thus restricting its broad application for on-chip analyte preconcentration, seawater desalination, and electrochemical analysis.

Motivated by the groundbreaking work of Sinwook and Yossifon [57], it would be interesting to test the feasibility of the enhanced treatment, instead of the linear approximation,

in reconstructing the various physical phenomena that may occur during the dynamic evolution of depleted DBL. In the ET-based micro/nanofluidic hybrid network, by inducing well-controlled ET vortex flow field at the anodic interface of the perm-selective membrane, propagating behavior of DBL can be flexibly adjusted via the interaction of an externally-imposed temperature gradient with the current flux. To this end, two microscale thin-film resistive heaters are embedded on the bottom surface of the anodic compartment, which are simultaneously activated to actuate ET fluid rolls. This pair of microheaters, with each having an equal length of 25 μm , are positioned at 500 and 700 μm away from the anodic interface, respectively, resulting in a 200 μm separation between them. The improved microscopic model is then used for accurately predicting the induced free charge and ET body force, when the depletion layer passes over the top of the microheaters imposed with different amount of thermal flux. Both microchambers are $L_M = 5$ mm in length, $H_M = 750$ μm in height, and $W_M = 10$ mm in width, and the ion-selective medium located at the center has an effective height of $H_N = 200$ nm and a physical length of $L_N = 1$ mm.

2.2 Mathematical model

In this study, the phenomenon of ET flow is accounted for in terms of transient electrokinetic transport of ionic species inside inhomogeneous liquid medium as a consequence of non-uniform heating. Gauss law establishes the intrinsic relationship between space charge density (ρ_f) and concentration field of ions [59]:

$$\rho_f = -\vec{\nabla} \cdot (\epsilon \vec{\nabla} \phi) = -\vec{\nabla} \epsilon \cdot \vec{\nabla} \phi - \epsilon \vec{\nabla}^2 \phi = F(c_1 - c_2) \quad (1)$$

where ϕ is the electrostatic potential, $\vec{E} = -\vec{\nabla} \phi$ is the electric field, ϵ is the liquid dielectric permittivity, F is the Faraday constant, c_1 is the concentration of positive ions K^+ , and c_2 is the concentration of negative ions Cl^- . For binary symmetric electrolyte of 1:1 monovalent ionic species, e.g., KCl, the motion of cations and anions obey the Nernst-Planck equation in terms of mass conservation [60]:

$$\frac{\partial c_1}{\partial t} + \vec{\nabla} \cdot \vec{J}_1 = 0 \cdot \text{with} \cdot \vec{J}_1 = \mu F c_1 \vec{E} - D \vec{\nabla} c_1 + \vec{u} c_1 \quad (2)$$

$$\frac{\partial c_2}{\partial t} + \vec{\nabla} \cdot \vec{J}_2 = 0 \cdot \text{with} \cdot \vec{J}_2 = -\mu F c_2 \vec{E} - D \vec{\nabla} c_2 + \vec{u} c_2 \quad (3)$$

where μ denotes the EPM of ions in electric fields, D the thermal diffusivity of charge carriers, and \vec{u} the flow velocity vector. \vec{J}_1 and \vec{J}_2 are the current flux due to the flow of positive and negative ions, respectively. They are both comprised of three distinct terms, including electromigration, diffusive and convective charge transfer. It is noteworthy that, for standard binary symmetric electrolyte, such as KCl, which has monovalent ionic species of K^+ and Cl^- used in present theoretical analysis, chemical reaction in the bulk fluid can be ignored due to its stable chemical content. In addition, the electric field intensity used for the ACET pump does not reach

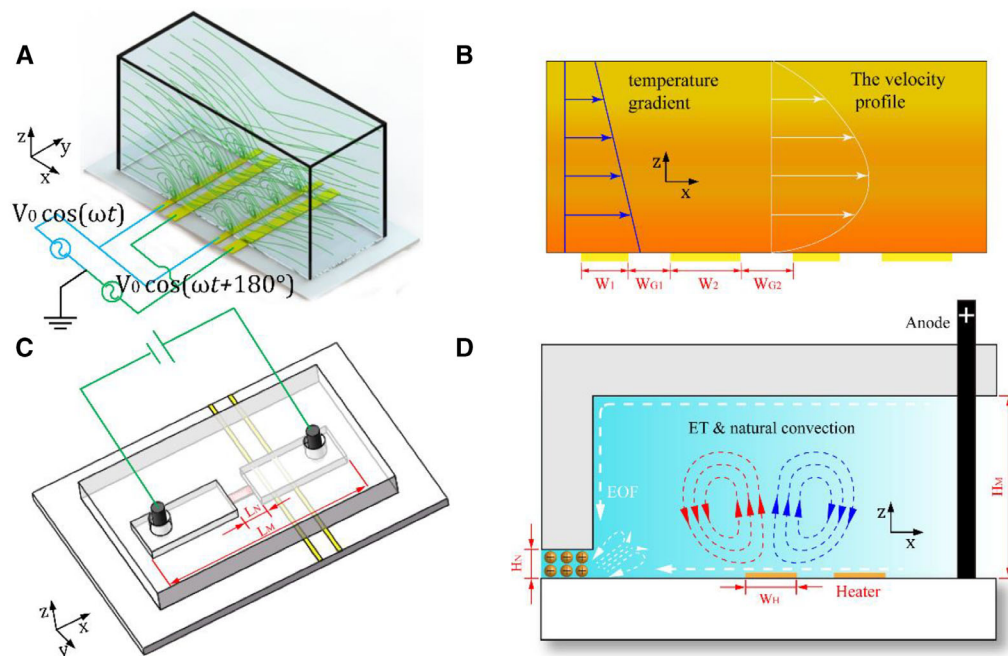


Figure 1. 3D schematic diagrams for the two fluidic devices discussed in current work. (A–B) A standard ET micropump embedding an asymmetric array of metal electrode strips (device #1), transports fluids unidirectionally from the narrower electrode to the wider counterpart due to symmetry breaking in Maxwell–Wager interfacial polarization. This device configuration is aimed at demonstrating the superiority of the microscopic physical description in the calculation of ET flow behavior. (C–D) A micro/nanofluidic hybrid system (device #2), where two microchambers on both sides surround a cation-selective nanoporous membrane located in the center. An external current source provides a constant overlimiting current density across the system, which induces ion depletion at the anodic membrane interface. The wavefront of depleted boundary layer propagates toward the source terminal by ion diffusion. Once two microscale heaters embedded at the channel bottom are actuated, flexible control of ion current transport is achievable once the IDZ passes over the heating elements due to convective mixing from both ET and NC.

the level to engender splitting reaction of water molecules, which may continuously produce H^+ and OH^- within the ion depletion zone in the over-limiting current regime in a nanofluidic ICP device. In view of this, it is not necessary for us to include bulk reaction terms in Eq. (2).

Aqueous solution is chosen here as the buffer medium, so the flow field is determined by Navier–Stokes equation for incompressible Newtonian fluid [21]:

$$\rho \frac{\partial \vec{u}}{\partial t} + \rho (\vec{u} \cdot \nabla) \vec{u} = \nabla \cdot \left[-p \vec{I} + \eta \left(\nabla \vec{u} + (\nabla \vec{u})^T \right) \right] + \vec{F} \quad (3a)$$

$$\nabla \cdot \vec{u} = 0 \quad (3b)$$

where $\rho = 1000 \text{ kg/m}^3$ denotes the mass density of liquid, p the hydraulic pressure, \vec{I} the unit tensor, η the medium dynamic viscosity, and \vec{F} any possible external force acting on each liquid element. In current analysis, we consider convective mixing due to ET and NC:

$$\vec{F} = \vec{F}_{ET} + \vec{F}_{NC} = \rho_f \vec{E} - \frac{1}{2} \vec{E} \cdot \nabla \vec{E} \epsilon(T) + \rho \beta g \vec{e}_z (T - T_0) \quad (4)$$

where \vec{F}_{ET} and \vec{F}_{NC} denote the ET body force and buoyancy force density, respectively. $\beta = 2.07 \times 10^{-4}/K$ is the thermal expansion coefficient, $g = 9.8 \text{ m/s}^2$ is the magnitude of gravity acceleration, T is the local temperature, and T_0 is the ambient temperature. The three terms on the right hand side of Eq. (4) represent the Coulomb force due to the induced free charge, dielectric force acting on polarized bound charge, and thermal buoyancy convection in sequence.

In the simulation experiment, all the medium physicochemical properties are functions of the temperature field T , except for its mass density of a constant value $\rho(T) = 1000 \text{ kg/m}^3$ [61]:

$$\eta(T) = 0.3808 - 0.0043T + 1.900 \times 10^{-5} T^2 - 3.6736 \times 10^{-8} T^3 + 2.6667 \times 10^{-11} T^4 \quad (5a)$$

$$\epsilon(T) = \epsilon(T_0) (1 + \alpha (T - T_0)) \cdot \text{with } \alpha = -0.004/K \quad (5b)$$

$$k_f(T) = k_f(T_0) (1 + \gamma (T - T_0)) \cdot \text{with } \gamma = 0.02/K \quad (5c)$$

$$D(T) = \frac{k_B T}{6\pi\eta(T)r} \quad (5d)$$

$$\mu(T) = \frac{q}{6\pi\eta(T)rF} \quad (5e)$$

$$\sigma(T) = \mu(T) F (c_1 + c_2) \quad (5f)$$

where k_f is the thermal conductivity of water, $r = 0.1$ nm is the radius of currently-used ionic species, and σ is the liquid electric conductivity. These parameters have a set of definite values at the temperature of reference $T_0 = 293.15$ K, including:

$$\begin{aligned} \eta(T_0) &= 0.001 \text{ Pa} \cdot \text{s}, \quad \epsilon(T_0) = 80\epsilon_0 = 7.0834 \times 10^{-10} \text{ F/m}, \\ k_f(T_0) &= 0.6 \text{ W/(m} \cdot \text{K)}, \quad D(T_0) = 2.15 \times 10^{-9} \text{ m}^2/\text{s}, \\ \mu(T_0) &= 8.8 \times 10^{-13} \text{ s} \cdot \text{mol/kg, and, } \sigma(T_0) = 0.1528 \text{ S/m.} \end{aligned} \quad (6)$$

for $c_0 = 10 \text{ mM}$

where $\epsilon_0 = 8.85 \times 10^{-12} \text{ F/m}$ denotes the vacuum permittivity.

To obtain the coordinate-dependent liquid properties, we have to solve the energy balance equation for the temperature field within the whole microfluidic device:

$$\rho C_p \frac{\partial T}{\partial t} + \rho C_p \vec{u} \cdot \vec{\nabla} T = \vec{\nabla} \cdot (k_f \vec{\nabla} T) + \sigma(T) \vec{E} \cdot \vec{E} \quad (7)$$

where C_p is the heat capacity, and $\sigma \vec{E} \cdot \vec{E}$ is the source term caused by Joule medium heating. In terms of a small Peclet number, contribution of thermal convection is much smaller than that of Fourier heat conduction, so the temperature equation is readily reduced to the steady-state form:

$$\vec{\nabla} \cdot (k_f(T) \vec{\nabla} T) + (\mu(T) F (c_1 + c_2) \vec{E} \cdot \vec{E}) = 0 \quad (8)$$

3 Results and discussion

3.1 Model comparison

We first demonstrate the general merit of our microscopic physical description, by comparing the ET pump behavior predicted from it and the classical model. As shown in Fig. 1A and B, geometric size of the target micropump is chosen with $W_1 = 40 \mu\text{m}$, $W_2 = 120 \mu\text{m}$, $W_{G1} = 50 \mu\text{m}$, $W_{G2} = 390 \mu\text{m}$, and $H = 500 \mu\text{m}$. The KCl electrolyte has a background salt concentration of $c_1 = c_2 = 10 \text{ mM}$. The electrokinetic chip is supposed to have a $100 \mu\text{m}$ thick PDMS lid and a $500 \mu\text{m}$ thick silicon substrate.

3.1.1 Boundary conditions

When taking a series of temperature-dependent liquid properties into account, Eqs. (1)–(3) and (5b) have to be calculated in a fully coupled manner with a transient solver.

3.1.1.1 B.C. for the electric field

A harmonic AC voltage signal of $V = V_0 \cos(\omega t)$ is imposed to the asymmetric electrode pair; periodic boundary conditions (B.C.s) are applied at two sides of the computational domain; normal current density vanishes on all other walls. The field frequency $f = \omega/2\pi$ is fixed at 100 kHz , so as to access the flow field of ET in the low-frequency limit, which is located between the inverse resistance times capacitance (RC) time scale for capacitive charging of the induced double layer (IDL) at the electrode surface and the charge relaxation time

of liquid volume for onset of bulk ionic screening. Out of this frequency scope, ET transport of bulk fluid would be weakened by either field-induced Debye screening at the ideally polarizable surface or instantaneous relaxation of ionic charge within each time-limited AC voltage circle.

3.1.1.2 B.C. for mass conservation

Electrochemical reactions are very likely to take place at the voltage used in the paper. In fact, the characteristic relaxation frequency of counterionic charge within the IDL at the electrode/electrolyte interface is given approximately by $f_{RC} = \sigma \lambda_D / 2\pi \epsilon W_{G1}$. For the ACET micropump, with the parametric space of $c_0 = 10 \text{ mM}$, the Debye length $\lambda_D = 3 \text{ nm}$, $\epsilon = 7 \times 10^{-10} \text{ F/m}$, $\sigma = 0.153 \text{ S/m}$, $W_{G1} = 50 \mu\text{m}$, f_{RC} equals 2.09 KHz . So, for field frequencies far beyond the reciprocal RC time scale $f_{RC} = 2.09 \text{ KHz}$, the voltage drop across the IDL would be negligibly small, and the same holds true for charge production from electrode kinetics as well as AC electroosmotic slip on the ideally polarizable surface [53, 62]. It is noteworthy that EO effect becomes even weaker with increasing liquid electrical conductivity whatever the applied field frequency is, due to a possible ion overcrowding effect within the IDL of a finite Debye length [52, 63].

However, since current analysis focused on the frequency range exceeding the inverse RC time scale $f_{RC} = \sigma \lambda_D / 2\pi \epsilon W_{G1}$ and below the threshold for onset of bulk ionic screening $f_{MW} = \sigma / 2\pi \epsilon$, the combined effects of electrode polarization and Faradaic reaction play a minor role and are hence safely disregarded in present work. Here, λ_D denotes the Debye screening length. In view of this, constant concentration value of $C_1 = C_2 = C_0 = 10 \text{ mM}$ is imposed on the ideally polarizable surface of these metal strips as well as the channel top wall. Any normal component of ion flux is forbidden at other insulating walls. Periodic B.C. is assumed on both sides. For extension of current theory to include the effect of Faradaic current injection, it is possible to achieve this by referring to Ref. 64, wherein the normal ion flux at the electrode surface is proportional to the exchange current density that is specifically related to the transient Stern layer voltage drop by the dynamic Butler–Volmer equation. At the same time, the total current density, i.e., the electrical displacement vector (since the reaction current also relays one another across the specific Helmholtz plane) is continuous at the diffuse/Stern layer interface.

3.1.1.3 B.C for flow field

The fluid motion is considered to manifest as a repetitive feature from one calculation cell to another. Besides, due to the usage of oscillating AC voltage signals, linear EO time-averages to zero at high field frequencies, and hence it is overlooked in the simulation study of case 1. For such, no penetration and no slip are designated on all the channel walls.

3.1.1.4 B.C. for temperature field

Ambient temperate of $T = T_0$ is stipulated on the top surface of PDMS lid and the bottom surface of Si substrate. Electric heat generation is included in the fluid bulk, while the thermal convection effect can be safely disregarded. By

integrating the control equation, continuity of temperature and normal thermal flux has to be satisfied at the PDMS/liquid interface as well as the liquid/Si interface of piecewise constant thermal conductivity across the phase boundary. Just as other fields, we still apply periodic B.C. on both ends of the calculation domain considering the spatial periodicity.

So, the influence that heat transfer through the microchannel sides has on the microflow fields is properly reflected by the conjugating condition imposed at those sharp material interfaces. All the thermal B.C.s are typical of such devices used by previous researchers, so are the thermal conductivities of various materials including $k_{\text{water}} = 0.6 \text{ W/m}\cdot\text{K}$, $k_{\text{Si}} = 140 \text{ W/m}\cdot\text{K}$ and $k_{\text{PDMS}} = 0.2 \text{ W/m}\cdot\text{K}$ [33, 65, 66].

More importantly, the same thermal B.C.s are applied for the classical linear model and the enhanced treatment, making the simulation results from both numerical treatments comparable.

3.1.2 Characterization of the pump flow field

The calculation results from the improved microscopic interpretation are shown in Fig. 2, with the device subjected to a fixed voltage amplitude $V_0 = 9 \text{ V}$. The time-averaged flow field behaves as an asymmetric pair of microscale eddies that rotate in opposite directions under DC limit. As shown in Fig. 2A, the flow vortices in the saline solution stream straight downward right above the center of the interelectrode gap, sweep tangentially across the conducting surface, and eventually meet one another to form closed fluid loops. Due to the symmetry breaking in electrode configurations, the fluid path is characterized by zigzag streamlines along the channel length direction on the global scale, and there is an observable pump flow component transporting unidirectionally from the narrower electrode to the wider counterpart. The bulk ET flow has the fastest pump speed just above the electrode surface, mainly due to the presence of a viscous boundary layer at the electrolyte/wall interface.

In the positive half cycle of the exciting sinusoidal voltage, appreciable electric field lines are emitted from the surface of narrower electrode (Fig. 2B), owing to the fact that the impedance of liquid medium is orders of magnitude larger than that of the metal leads for external wire connection. According to the conservation of total current density, the field lines enter and intersect the surface of wider electrode at right angles. Consequently, the major path via which the current is transmitted is the liquid phase interconnecting the oppositely-polarized electrode bars. For the negative half cycle, the only difference in ion transport state is a reversal in the direction of electrophoretic translation.

Considering the strong electric field strength within the gap region, the temperature attains maximum value of 294.45 K on top of the electrode pair, implying a temperature elevation of 1.3 K produced by electric heat generation in the bulk phase (Fig. 2C). In order for both Gauss law and current continuity condition to be satisfied at the same time, the interaction of the internal temperature gradient with the

electrical current induces smeared spatial charges (both free and bound) inside the fluid domain of anisotropic electric properties. These induced harmonic charges are in turn pushed by the same-frequency oscillating electric field to exert a nonlinear DEP body force on the liquid volume, which scales with the voltage squared and thereby survives well in alternating fields. So, ET convection is in fact the DEP motion of liquid phase in a continuous conductivity gradient. The DEP force acting on each liquid element tends to drag the fluid of higher polarizability on top of the electrode pair (due to a larger conductivity from peak temperature elevation) to the vicinity of the electrode edge, where the local field intensity becomes largest, so as to maximize the system electric energy.

In this way, ET convection of fluids can be well compared with DEP translation of colloidal particles exposed to an electric field gradient, wherein the in-phase component of DEP force invariably delivers the latex beads of higher (lower) polarizability to (away from) the field source and sink, termed as positive-DEP (negative-DEP). The situation shown in Fig. 2A is in effect the positive-DEP motion of fluid flows in a bulk conductivity gradient. At higher field frequencies, since the displacement current dominates over ion conduction, the negative-DEP body force of a dielectric polarization origin pushes the fluid of lower permittivity inside the gap away from the electrode surface to the channel top wall. The working distance of high-frequency ET vortex flow field is quite limited, however, the device cannot efficiently pump fluidic samples any longer. To this end, we only focused on low-frequency pump behavior driven by ET mechanism.

3.1.3 Quantitative studies

Since the classical model is derived by linear perturbative expansion, it is a highly efficient macroscopic approximation. It forms stark contrast with current improved treatment, which is justifiable from microscopic physical argumentation. In this way, the two models stand for the two extreme aspects of the physical description of ET-induced flow, and it would be of great importance to make a comparison study between them. To this end, taking advantage of both the models, the pump flow rate of ET is quantified and compared in Fig. 3A as a function of the imposed field strength.

As shown in Fig. 3A, when the applied voltage is no more than 7 V ($V_0 \leq 7 \text{ V}$), which corresponds to an upper limit of $E_B = 140 \text{ V/mm}$ for average field intensity across the narrow slit, both numerical approaches present an identical device performance, due to a weak field-induced smeared structural polarization within the low-voltage limit. As the voltage amplitude reaches and even exceeds 9 V, calculation results from the two distinct approaches deviate more appreciably from one another, in that the linear approach always predicts a higher flow rate than the improved physical description (Fig. 3A).

According to Fig. 3B, we obtain same temperature elevation inside the liquid bulk from both the models, which grows quadratically with the field strength. It takes

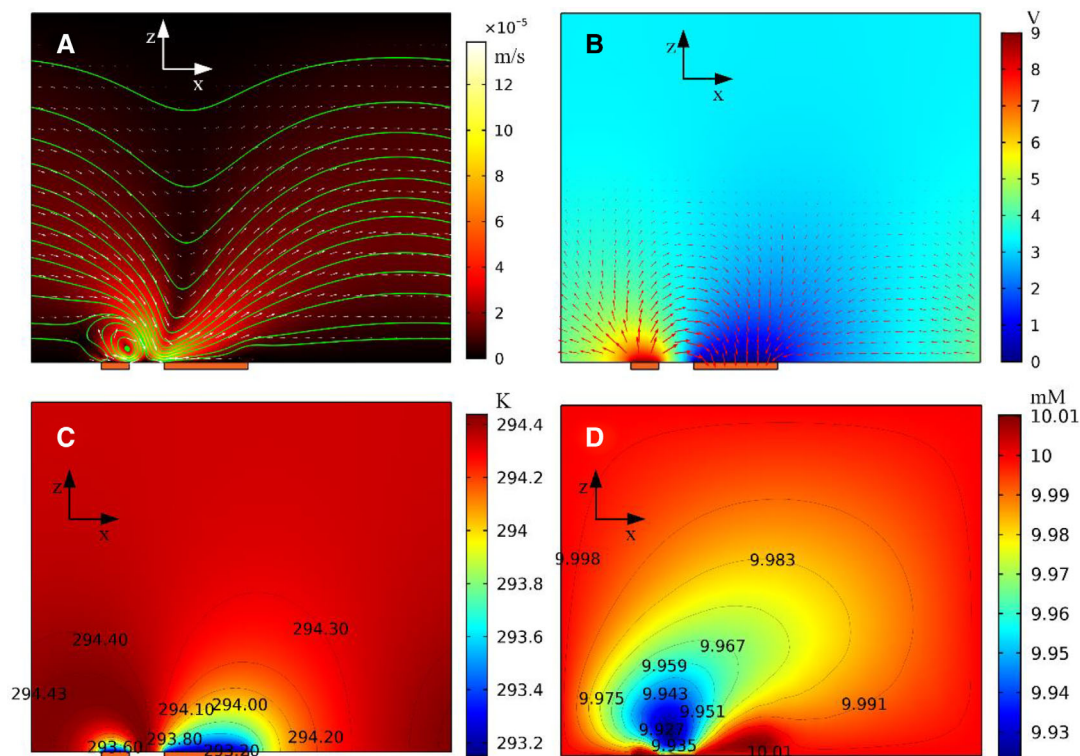


Figure 2. Simulation result of various field variables in an ET micropump taking advantage of asymmetric electrode arrays, under a given parametric space of voltage amplitude $V_0 = 9$ V, background ion concentration $C_0 = 10$ mM in the low-frequency limit. (A) A surface, arrow and streamline plot of time-averaged ET fluid motion (unit: m/s); (B) A surface plot of voltage amplitude and an arrow plot of electric field at the peak time point (unit: V); (C) A surface and contour plot of temperature field due to time-averaged Joule medium heating (unit: K); (D) A surface and contour plot of nondimensional salt concentration $c = (c_+ + c_-)/2c_0$ at the time node when the peak field intensity appears.

at most a value of 2.3 K, implying a maximum rise of liquid conductivity by 5.28% when the voltage is below 12 V. So, it is not possible to use the nonlinear source term of electric heat generation to account for a one-fifth decay in pump performance estimated by the enhanced treatment (Fig. 3A).

We then resort to the concentration distribution of ion species in the bulk phase. A vivid plot of concentration field at the time point of peak voltage is displayed in Fig. 2D, while it is worth to note that the salt concentration is not static at all and also oscillates synchronously with the AC forcing. Concentration perturbation becomes most severe on top of the electrode gap, where minimum concentration appears as a consequence of inhomogeneous ion transport (Fig. 2D). In fact, when considering the continuity of electric current density $\vec{\nabla} \cdot (\mu(T)F(c_1 + c_2) \vec{E}) \approx 0$, the number density of charge carriers $c_1 + c_2$ has to decay to certain extent for accommodating the rise in EPM in heated regions. The suppression of salt concentration may indirectly exert an adverse influence on the induced free charge density.

As shown in Fig. 3C, the enhanced theory forecasts an observable deviation of local ion number density, while no such variations are obtainable from the linear perturbation analysis. As the applied voltage goes up, the fluctuation of ion concentration distribution becomes more conspicuous, due

to the increase in the peak value of EPM (Fig. 3C). The unexpected suppression of salt concentration by intense Joule medium heating results in a decrease of the induced free charge density (Fig. 3D), which is linearly proportional to the concentration difference between cations and anions according to Gauss law. This leads to a smaller ET body force for the enhanced treatment compared to the linear approximation, and the same also holds true for the ET flow field.

The research group of Wu has previously reported the ET pump rate measured in practical experiments is always smaller than simulation results [56]. In a recent study of induction EHD, we have developed a fully-coupled model incorporating potent thermal-electric interaction. However, it even presents a higher electrokinetic flow velocity than the linear treatment in cases of strong temperature gradient. For this reason, the overestimation of ET fluid motion by theoretical analysis is still an intractable problem needing an urgent solution. To this end, though the improved physical description predicts a worse pump performance, it is much closer to experimental results for moderate voltages. Considering microscopic laws, the occurrence of subtle variation in salt concentration is clearly adjacent to the electrode spacing for fluids undergoing Maxwell–Wagner structural polarization. This tends to evacuate the induced charge wave,

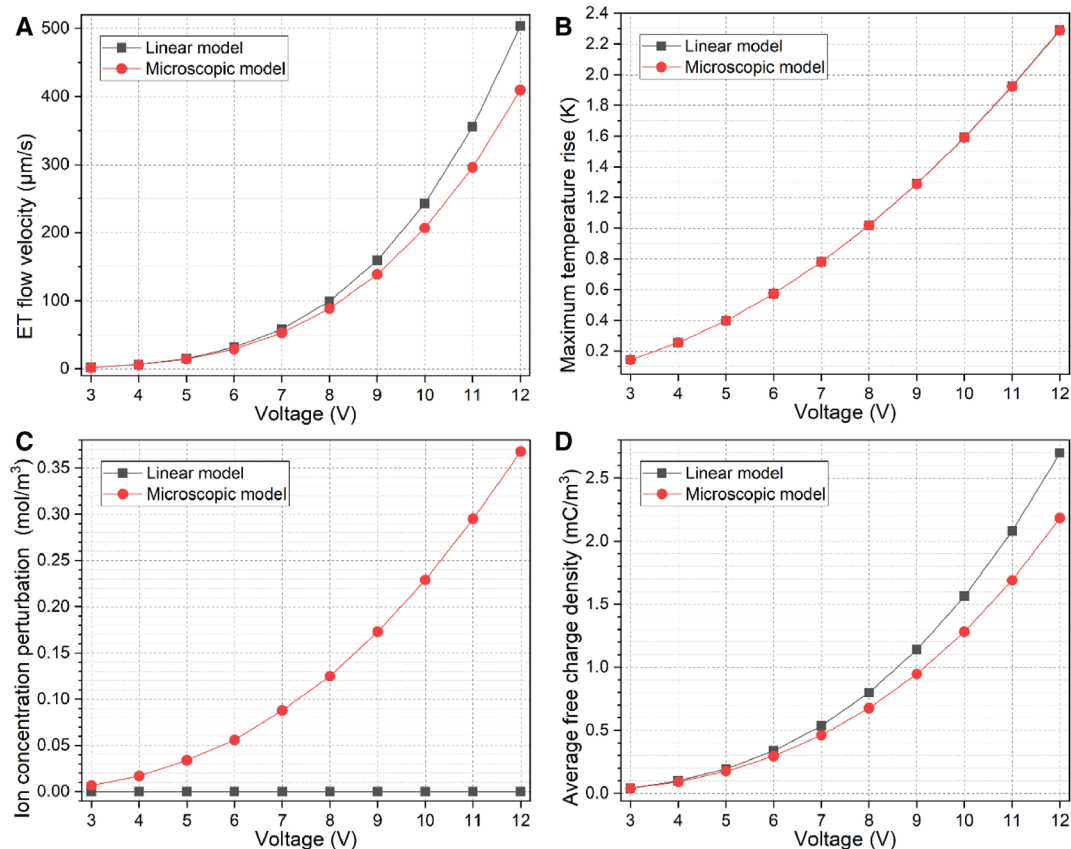


Figure 3. A comparison study between the classical linear model and the enhanced microscopic treatment with respect to a typical ET micropump as a function of the applied voltage. (A) Voltage-dependent ET pump flow rate; (B) Voltage-dependent maximum temperature elevation within the buffer medium; (C) Voltage-dependent steady-state concentration deviation from the initial value; (D) Voltage-dependent free charge density induced by smeared interfacial polarizations.

decrease the Coulomb body force and therefore inhibit the ET rate of flow. In this way, by ensuring the conservation laws in microscale that have not been used for interpreting ET so far, our enhanced treatment sheds insightful light on the unexpected overestimation of ET flow velocity from those previous models. Most importantly, it makes the simulation results further approach the practical experiment.

3.2 ET-based control of ion current transport

The accuracy of the improved physical description has been demonstrated in previous section in terms of the resulted device performance of a typical ET pump, which reflects its superiority over the traditional linear approximation. In the context of this microscopic treatment, salt concentration in the absence of any applied voltage has a uniform distribution within the BGE. Under this premise, an AC signal imposed to the electrode array can induce gradients in ion density within high-temperature region of a relatively larger EPM, accounting for a smaller ET flow rate versus the classical model. In practice, however, a perturbation of background salt concentration may intrinsically pre-exist in microscale devices for some common reasons. For instance,

the phenomenon of ICP induced by an external additional electric field imposed across an ion-selective medium, the sharp material interface between electrolytes of different ion concentration, and an externally imposed ion concentration gradient across the electrolytic ports, are all typical examples for this. With appreciable non-uniform heating, such dielectric gradient from initial concentration variation may coexist with that due to temperature-dependent electrical properties. Both factors are strongly coupled to one other, resulting in an even more complicated ion density field and the consequent transient state of ET convection.

From above analysis, the scientific robustness of the improved approach can be well reflected by model simulation for device designs having concentration gradients in the early time. Inspired by this, a micro/nanofluidic hybrid system displayed in Fig. 1C and D is employed in current analysis for a vivid visual clarification of our model's general applicability even when strong ICP takes place.

3.2.1 B.C.s

Since external heating dominates electric heat generation, the energy problem is decoupled from the electrostatic and mechanical problem. Accordingly, we first calculate the

thermal conduction equation with a stationary solver. Once those temperature-dependent material properties are known, the electric field, ion transport, and fluid flows are solved in a fully coupled way by using a transient solver.

3.2.1.1 B.C. for electric field

A constant current source $i_{app} = 1.45i_{lim}$ is imposed at the right edge of the anodic chamber in terms of an equivalent electric displacement vector $\vec{D}_{elec} = -\epsilon(RT/F)(1/2FDc_0)i_{app}\vec{e}_x$. Here $i_{lim} = 2DFc_0/L_M$ is the overlimiting current density of our device design. Donnan potential, $\phi(T) = -RT/F \cdot \ln(N)$, is imposed at the anodic membrane surface. Complete Debye screening, $\vec{n} \cdot \vec{\nabla} \phi = 0$, is imposed in the bulk fluid right outside the electrical double layer on all the insulating charged walls.

3.2.1.2 B.C. for temperature field

An identical heat flux density $-k_f \vec{\nabla} T \cdot \vec{n} = Q_s$ is imposed on the surface of both thin-film resistive microheaters, which are embedded at the channel bottom. Ambient temperature is fixed at the source terminal. In addition, we make use of an equivalent form of B.C. on the PDMS/liquid interface, glass/electrolyte interface, and sidewall/fluid interface to describe the actual thermal field inside the saline solution, which is given as follows [67]:

$$(T - T_0) / R_s = -k_f \vec{\nabla} T \cdot \vec{n} \quad (9)$$

where R_s denotes the thermal resistance per unit area, and $T_0 = 293.15$ K the ambient temperature.

- At the upper PDMS membrane, $R_{s,PDMS1} = t_{PDMS1}/k_{PDMS} + 1/h$, is comprised of both conduction and convection factors in series, with the insulation layer thickness $t_{PDMS1} = 3$ mm, PDMS thermal conductivity $k_{PDMS} = 0.2$ W/m/K, and heat-transfer coefficient of $h = 10$ W/m²/K resulting from external NC.
- At the channel bottom surface interfacing a glass substrate of thickness $t_{glass} = 500$ μ m and heat conductivity $k_{glass} = 1$ W/m/K, and at the channel side wall with thickness $t_{PDMS2} = 1$ mm, we merely account for the thermal resistances from Fourier heat conduction, that is, $R_{s,glass} = t_{glass}/k_{glass}$ and $R_{s,PDMS2} = t_{PDMS2}/k_{PDMS}$.

3.2.1.3 B.C. for mass conservation of ion motion

The concentration of cations and anions is maintained constantly at the initial value $c_+ = c_- = c_0 = 10^{-5}$ mM in the anodic port. The normal flux of negative ions vanishes at all other liquid/solid interfaces. It is assumed that the ion-exchange medium is ideally cation-selective, that is, its inner walls are negatively charged and hence preferentially conduct positive ions while any axial motion of co-ions is forbidden. Accordingly, the concentration of cations is kept at a relatively high value of $c_+ = Nc_0$ ($N = 10$) near the membrane surface, whereas anions meet impenetrable conditions at the same place.

3.2.1.4 B.C. for fluid mechanics

The anodic entrance is set as an open boundary for fluid motion. Since a constant DC current source is applied across the two electrolytic ports shown in Fig. 1C, the net effect of EO on convective transport of ion species cannot be neglected. In this sense, linear EOF is reflected by imposing the Helmholtz slip formula at the solid surface in direct contact with liquid medium, that is, $\vec{u}_{slip} = -\epsilon \zeta \vec{E}_t / \eta(T)$, where $\zeta = -50$ [mV] denotes the native zeta potential, and \vec{E}_t the tangential electric field vector. As for channel walls adjacent to the membrane, we have imposed no slip and no penetration for a possible Coulomb force within the extended space charge layer (ESCL), which may interfere with linear EO by inducing EI at the anodic membrane interface.

3.2.2 Convection modes

As shown in Fig. 4A, the surface heat flux Q emitted from the two thin-film resistive heaters results in an inhomogeneous temperature field across the anodic chamber. When no heat flux is applied to the microscale heating element ($Q = 0$), the temperature distribution has a constant value of ambient temperature $T = T_0$ everywhere in the microdevice, in that the ionic conductivity is too small to induce any observable electric heat generation. When both microheaters are actuated at the same time, however, thermal conduction

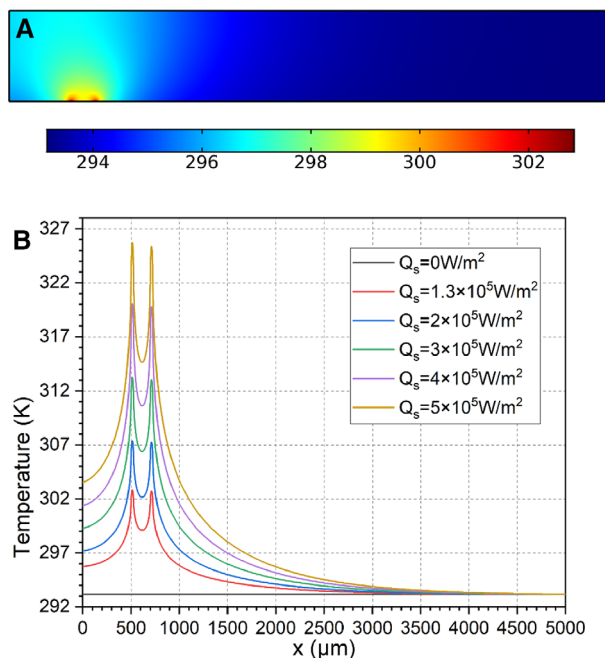


Figure 4. Simulation results of spatial temperature distribution within the anodic chamber interfacing an ion-selective medium, by taking advantage of equivalent B.C.s and temperature-dependent thermal conductivity of liquid. (A) A surface plot of temperature field in the anodic microchannel under an imposed heat flux Q at the surface of two adjacent microheaters; (B) Steady-state temperature distribution along the channel bottom surface.

reaches the steady state after a very short relaxation time, and the rise in temperature takes a maximum value just on top of the external heat source, with a double peak profile distributed along the channel bottom surface (Fig. 4B). As expected, the maximum temperature elevation increases linearly with an enhancement of the external heat flux Q_S from 0 to $5 \times 10^5 \text{ W/m}^2$ (Fig. 4B), and is always no more than 40 K, so it is impossible for water boiling to occur. Such a non-uniform temperature distribution from embedded heating elements gives rise to appreciable gradients in medium dielectric properties, which interact actively with the electric current flux to induce ET vortex flow field.

In fact, fluid motion is far more complicated than this simple picture. As indicated in Fig. 5, four different convection modes referring to pure EO, ET&EO, NC&EO, and ET&NC&EO, may affect the spatial-temporal evolution of IDZ to different extent. All the simulation results of fluid physics are taken at a same time node of $t = 0.72t_D = 9000 \text{ s}$ with the typical diffusion time $t_D = L_M^2/D = 12500 \text{ s}$, by inserting distinct body force terms into the Navier–Stokes equation, with EO slip always present on the channel walls. The fluidic channels have a sufficient vertical dimension of $H_M = 750 \mu\text{m}$, in stark contrast with the small height of nanoporous membrane $H_N = 200 \text{ nm}$. Otherwise, if the channel height is reduced and becomes no more than $500 \mu\text{m}$, the micro-vortices driven by

various mechanisms cannot be fully developed due to a vertical confinement effect, and therefore are not able to achieve an effective control of ion transport via convective mixing. When the two microscale heating elements are not activated with $Q_S = 0$, the sole convection mechanism is linear EO streaming, which is driven by the interaction of the applied current flux with the positive counterions inside the native double layer. Two symmetric eddies are induced just at the anodic membrane surface, and recirculated in opposite directions (Fig. 5A). The fluids eject toward the current source, which is in the direction of the translative motion of ion-depleted wave-front. In view of this, EO pumping aids the extension of DBL driven by ion diffusion against the membrane. Besides, the strength of EO fluid motion enhances progressively with time, in that the local field intensity increases incessantly with further dissipation of salts in IDZ (Fig. 6B).

For the sake of comparison, we then activate the two microheaters with an identical surface heat flux of $Q_S = 1.3 \text{ W/m}^2$. As the ion-depleted zone (as represented by the concentration contour of $c = 0.1$ in Fig. 7C) passes over the heating elements at $t = 9000 \text{ s}$, the in-situ electric field strength is augmented appreciably (Fig. 6A). It interacts positively with the imposed temperature gradient, and induces strong vortex flow field of ET around this critical time point, as shown in Fig. 5B. The transient ET whirlpools behave as a pair of counter-rotating micro-vortices throughout the channel depth direction. Fluids are dragged downward by ET body force above the surface of heaters, and rush to the membrane entrance to form closed loops. Under this situation, when the heating elements are embedded at the bottom of the anodic fluidic chamber, convective mass transfer of charge carriers is opposite to their diffusive transport, so the actuation of ET has a negative effect and would inhibit the dynamic growth of DBL by convective mixing.

As shown in Fig. 5C, thermal buoyancy convection in gradients of liquid mass density is also a possible factor for suppressing the length of ion-depletion layer. The rotating direction of vortex flow field caused by NC (Fig. 5C) is opposite to that from ET effect (Fig. 5B), in that fluid flows induced by NC stream upward on top of the two microscale heaters, which can stir the salt concentration as well.

The qualitative characterization of different convection modes presented above is insufficient to indicate the specific performance in ion-current rectification, so it is essential to conduct a quantitative analysis. The dynamic evolution of DBL resulting from different flow modes is displayed in Fig. 7B, in terms of the dimensionless concentration profile $c = (c_1 + c_2)/2/c_0$ along the channel top wall. Whatever the flow condition is, the length of ion-depleted zone invariably extends rightward as time advances, which is a direct consequence of ICP under over-limiting currents and may be accelerated by EO pump effect to some degrees (Fig. 5A).

When superimposing ET (Fig. 5B), NC (Fig. 5C), or ET plus NC (Fig. 5D) on EO, all can change the dynamic evolution state of DBL (Fig. 7B). At the early time of $t = 3000 \text{ s}$, the effect of NC on the depletion layer's growth is more important than that of ET (See the set of dash dotted lines in Fig. 7B),

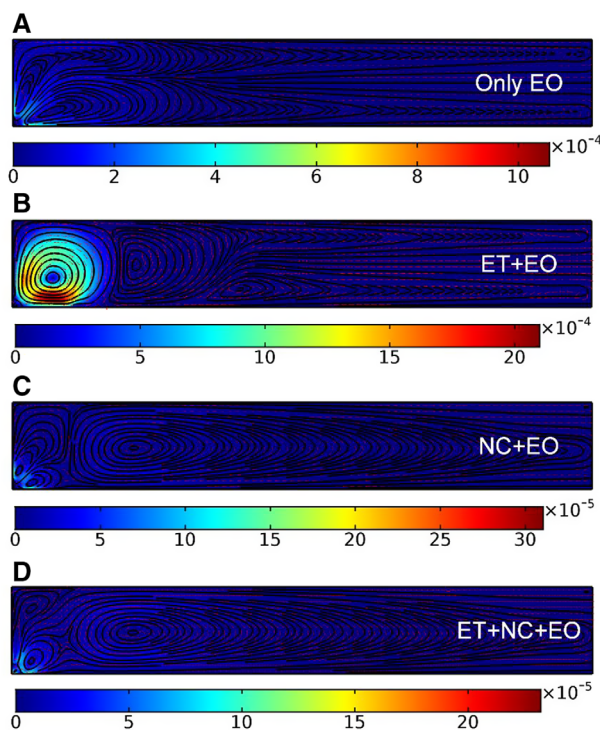


Figure 5. Different convection modes at $t = 9000 \text{ s}$ when the depleted wave-front passes over the two microscale heaters. (A) In case with only ET for zero imposed heat flux. (B–D) For an identical thermal flux of $Q_S = 1.3 \times 10^5 \text{ W/m}^2$, (B) when we consider ET together with EO slip, (C) when we consider NC together with EO slip, (D) when ET and NC are simultaneously considered in the flow field analysis (unit: m/s).

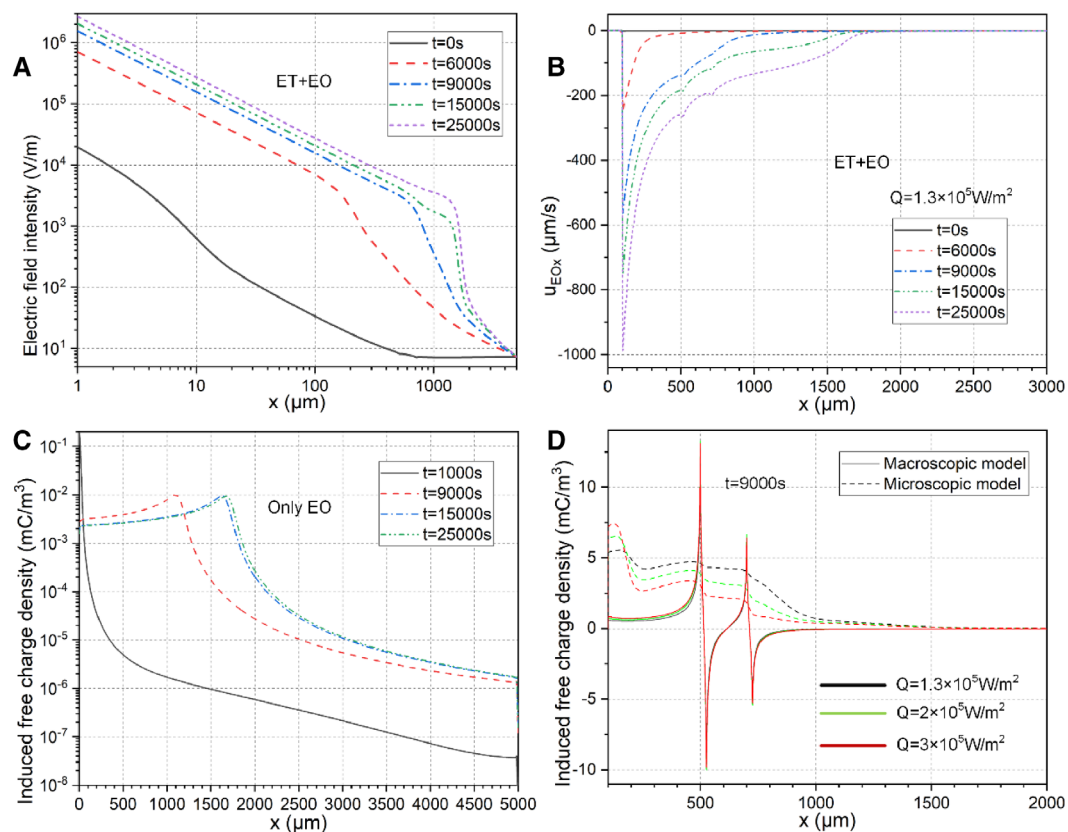


Figure 6. (A) Electric field strength as a function of the distance from the anodic membrane interface for different time points. (B) Electroosmotic slip velocity along the channel bottom under $Q_S = 1.3 \times 10^5 \text{ W/m}^2$ at different time nodes. (C) In the absence of any heat source ($Q_S = 0$), the x -dependent free charge density for different time points. (D) Effect of the imposed heat flux on the space charge density, which are obtained from classical model and enhanced microscopic treatment at $t = 9000 \text{ s}$, respectively.

in that the electric field adjacent to the two microheaters is too small to induce observable ET convection (Fig. 6A). As long as the ion-depleted wave-front passes over the surface of heating elements (See the dashed lines in Fig. 7B) at $t = 9000 \text{ s}$, convective mixing from ET is sharply enhanced by an increase in local field intensity by more than two orders of magnitude (Fig. 6A), while NC is kept constant in a similar temperature field as the initial stage of $t = 3000 \text{ s}$. When the time node reaches $t = 25000 \text{ s}$, the DBL almost stops propagating and reaches the steady state, and at this juncture, the vortex flow field from combined ET and NC (Fig. 5D) achieves an ideal control of ion current transport by producing well reinforced convective stirring (See the solid lines in Fig. 7B).

The influence that ET and NC have on the spatial-temporal extension of IDZ can be reflected by chronopotentiometric (voltage-time, or V-t) response as well. Applying a constant current flux of $I_{app} = 1.45I_{limit}$ across the fluidic system, which is 1.45 times the over-limiting current density, the voltage drop across the anodic chamber increases monotonously with time, and reaches the steady state for about $t = 25000 \text{ s}$. The applied current is enough to induce diffusive extension of DBL, which reduces the solution conductivity and increases the system electric impedance as the time advances. Since the dot product of impedance

and current determines the resultant voltage drop, it would increase as the DBL's wave-front further approaches the source terminal, and stop rising once the IDZ is fully developed in the eventual status (the black line in Fig. 7A).

When considering the suppression effect of ET and NC on IDZ extension, the voltage magnitude becomes smaller than the reference state (the red and blue lines in Fig. 7A). Under the condition with only ET, the voltage increases more slowly at $t \geq 9000 \text{ s}$ than the early phase (the red line in Fig. 7A), on account of an enhancement in electroconvective mixing as the local electric field strength near the heaters becomes sufficiently large. On the other hand, for NC, the slope of V-t curve is quite uniform along with the dynamic growth of DBL, because the flow field driven by NC is constant and independent of the transient electric field distribution (the blue line in Fig. 7A). Once the two effects of a same thermal origin emerge simultaneously, the growth rate of voltage is more severely suppressed by convective mixing (the green line in Fig. 7D).

Accordingly, in terms of the evolving concentration field and V-t response for various convection modes, ET has a definite influence on ion transport when microfluidics meets nanofluidics. The classical model of ET, however, cannot well predict such effect. As shown in Fig 6C, when no heat flux is supplied for $Q_S = 0 \text{ W/m}^2$, the microscopic physical

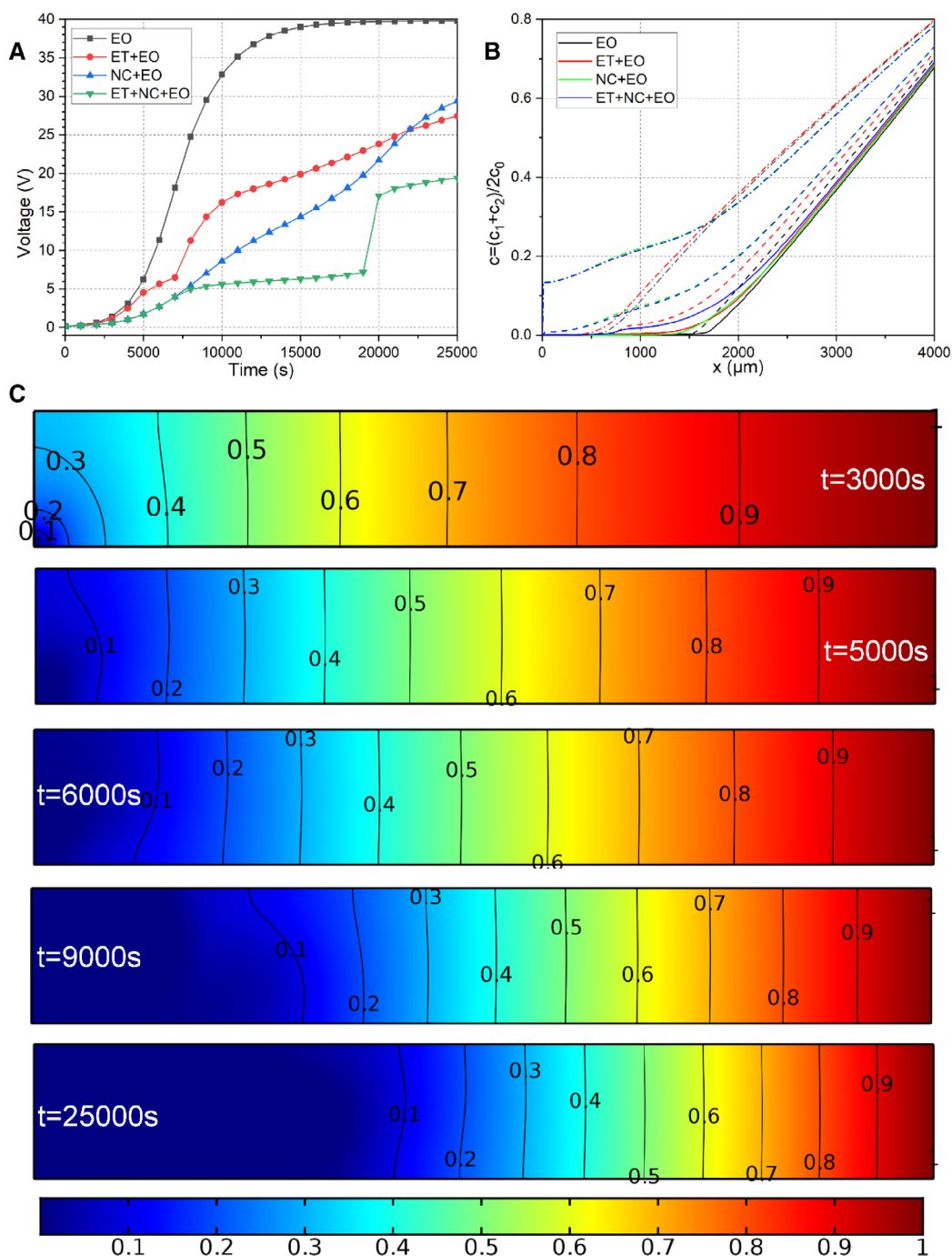


Figure 7. The spatial-temporal evolution of the depleted DBL in a temperature gradient. (A) The chronopotentiometric ($V-t$) response driven by the overlimiting current at $Q_S = 1.3 \times 10^5 \text{ W/m}^2$ under various convection modes, including EO, ET, NC, and ET+NC. (B) Time evolution of the DBL in terms of the dimensionless concentration distribution, along the channel bottom, where $t = 3000 \text{ s}$ for the dash dotted lines, $t = 9000 \text{ s}$ for the dashed lines and $t = 18000 \text{ s}$ for the solid lines. (C) Dynamic propagation of the ion-depletion layer as a function of time, in terms a surface and contour plot of $c = (c_1 + c_2)/2c_0$ inside the anodic chamber at different time nodes.

description presents an inhomogeneous distribution of induced free charge density along the channel length direction. The diffuse charge within ESCL exhibits a single plateau during the entire DBL propagation process (Fig. 6C). In fact, both the non-uniform ion number density within the IDZ and the

temperature-dependent material properties make contribution to the ultimate conductivity gradient that accounts for the ET effect. To this end, it is not possible for the classical model to predict any charge density in the anodic chamber, since the linear perturbation analysis has only considered

thermal anisotropy under uniform salt concentration, which is right against this particular circumstance with no heating but ion density fluctuation. As IDZ further expands with time, the wave-front of space charge layer induced by ICP moves in phase with DBL and becomes closer to the source terminal, as shown in Fig. 6C. It is worth to note that, we can only obtain such dynamic propagating behavior of ESCL via the enhanced treatment, while the classical model would malfunction. No EI occurs according to the calculation result for $Q_s = 0$, however, in that the charge density magnitude within the ESL is merely on the order of 0.01 mC/m^2 .

On switching these microscale heaters on, the macroscopic and microscopic model can both present a distribution of free charge density near the membrane surface for different imposed heat flux Q_s , as shown in Fig. 6D, albeit having completely different profiles. The enhanced model even estimates a larger charge density adjacent to the anodic membrane interface than the linear approximation for all time nodes (Fig. 8A–D). This amply demonstrates the robustness of the improved physical description, since the classical model cannot resolve the induced charge wave within the ESCL and thereby natively gets a smaller charge density. In this view, it is much more convincing to apply the microscopic model to describe physics of ET convection when salt concentration is not constant in space.

Besides, with larger heater powers, flow velocity of ET vortex becomes quicker in the early stage. At the same time, however, quicker ET convection produces more potent convective mixing effect on the dynamic growth of DBL. In this sense, the propagating speed of ion depletion layer would slow down at larger temperature elevation. This effectively reduces the system impedance, and hence decreases the voltage drop across the chamber length direction at a constant current source. Since the electric field intensity above the microscale heaters diminishes, the degree of Maxwell–Wagner structural polarization in a conductivity gradient is weakened as well, resulting in a decaying space charge density at a greater heat source, as shown in Fig. 6D.

In addition, the ionic charge density approaches $O(10) \text{ mC/m}^2$ at $t \geq 7000 \text{ s}$ (Fig. 8B–D) for $Q = 1.3 \times 10^5 \text{ W/m}^2$, which is about three orders of magnitude larger than $O(0.01) \text{ mC/m}^2$ without external heating (Fig. 6C). To this end, it is indeed the ET effect that causes convective mixing and achieves an active control of ion current transport in the anodic chamber, while EI is negligibly small for this situation.

3.2.3 Ion transport control with different heat flux

We then calculate both the V-t response and the dimensionless ion number density affected by ET with different heat flux imposed to the two microheaters, in Fig. 9A and B, respectively. As indicated clearly by these V-t curves in Fig. 9A, an enhancement in the imposed temperature gradient has the tendency to increase the salt concentration in IDZ in terms of inducing a smaller system impedance. That is, the stirring performance for ion species due to convective mixing from ET vortex flow field gets better in a larger temperature gra-

dient, which induces stronger Maxwell–Wagner interfacial polarization adjacent to the microheaters in terms of a subtle change in charge induction (Fig. 6D). The same conclusion is even vividly obtainable from Fig. 9B, where the dynamic length of ion-depletion layer is invariably made shorter with an increase of Q_s for the entire propagation process.

Importantly, our simulation results can qualitatively capture the salient feature of dynamic transport behavior of IDZ within a real nanofluidic ICP device developed in Ref.57. In this pioneering research on ET-based ion current control, it is demonstrated by practical experiments that ET vortex flow field is able to effectively stop the growth of DBL, which agrees well with current theoretical predictions shown in Fig. 7B and Fig. 9B.

3.3 Discussions on the impact of the enhanced model and relevant limitations

We focused on ET fluid motion at the micrometer dimension in this work. Indeed, a binary symmetric electrolyte KCl has been used all the time for demonstrating the superiority of the enhanced microscopic treatment. Even so, our improved model with more details can be well extended to study ET convection of other buffers and different background ion densities. For achieving this goal, bulk chemical reactions and surface Faradaic current injection should be incorporated in the renewed mathematical formulations, by adding bulk reaction terms in governing equation Eq. (2) and modifying the B.C. of normal ion flux considering field-induced exchange current density at the metal surfaces undergoing electrode polarization, respectively.

In the context of nonlinear electrostatics excluding linear EO streaming that time-averages to zero in AC fields, since ICEO appears at frequencies below the reciprocal RC time scale for IDL capacitive charging, current model that has ignored electrochemical polarization is only feasible in capturing the actual fluid dynamics of ET beyond the threshold frequency for onset of electrochemical ion relaxation. Besides, in the case of internal heating, the solution conductivity usually has to exceed 0.05 S/m for inducing sufficient electric heat generation for activating observable net time-averaged ET streaming in harmonic fields, or else ICEO plays a dominating role at negligibly small temperature elevation in the low-frequency limit. So, how to surmount these limitations inhibiting the wide applicability of this enhanced treatment would certainly serve as an important topic of our future research.

4 Concluding remarks

In short summary, we have presented herein both comparison study and application demonstration, to introduce a microscopic physical description of ET-induced flow. This new model for interpreting the physical origin of ET effect directly accounts for mass conservation of ions in electrolyte

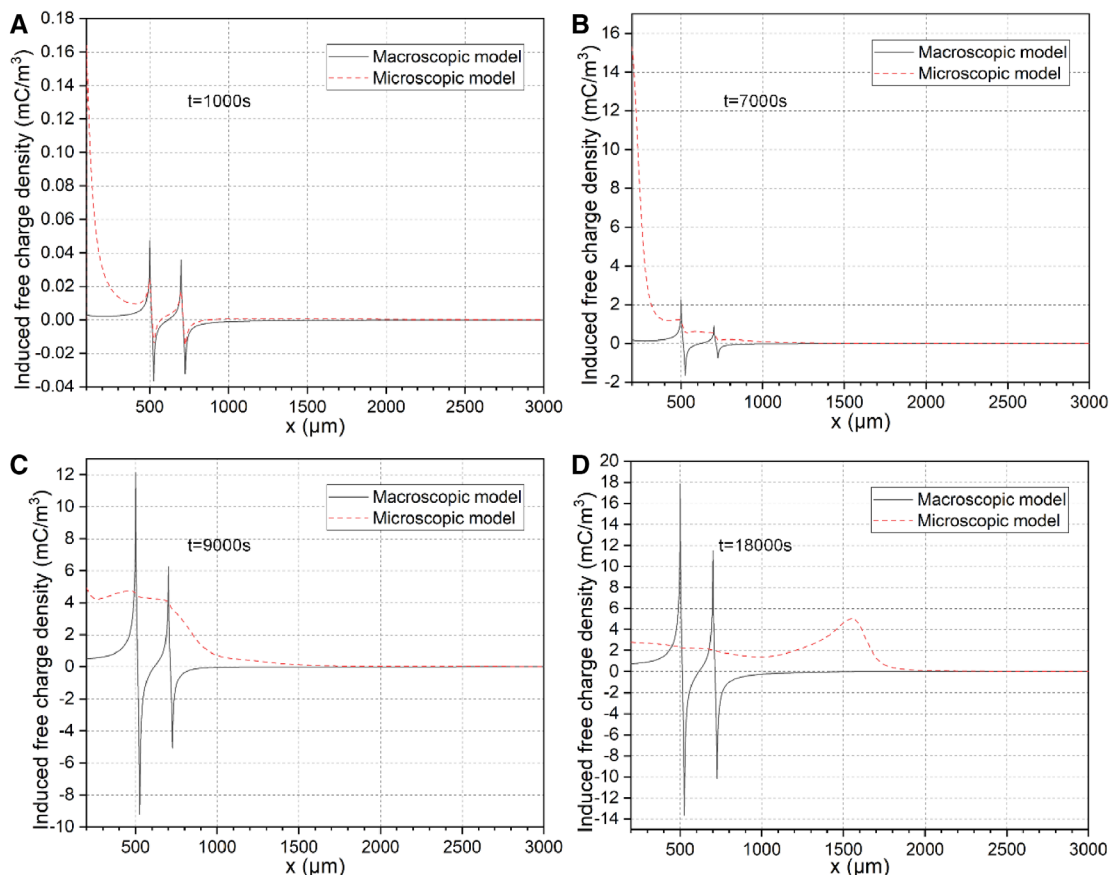


Figure 8. A comparison study on the induced charge density near the ion-selective medium, between the linear approximation and the microscopic physical description of ET effect, at different time points: (A) $t = 1000$ s, (B) $t = 7000$ s, (C) $t = 9000$ s, and (D) $t = 18000$ s.

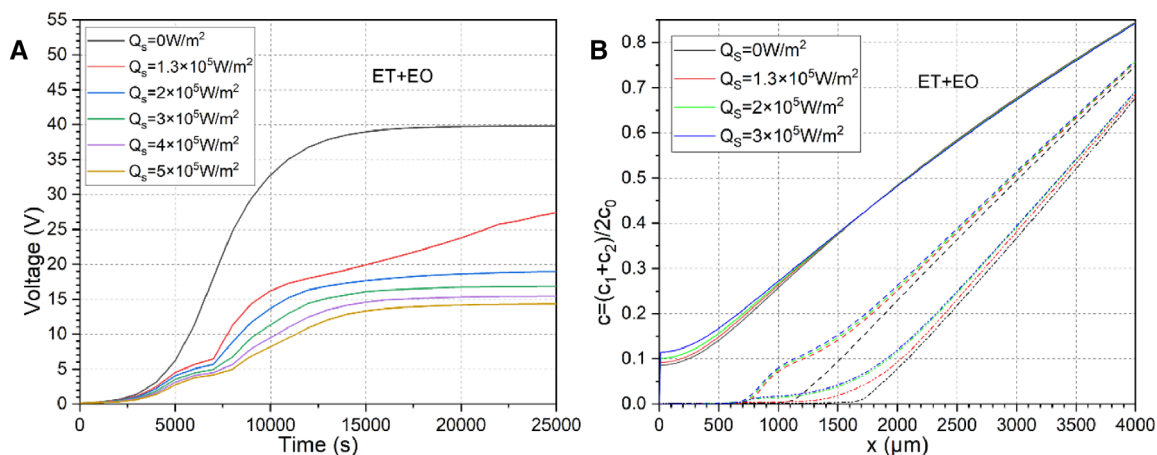


Figure 9. Effect of imposed heat flux on the dynamic evolution of the DBL due to ET. (A) V–t response for different heat flux. (B) Distribution of the dimensionless concentration along the channel bottom surface for different heat flux, where $t = 3000$ s for the solid lines, $t = 9000$ s for the dashed lines and $t = 18000$ s for the dash dotted lines.

with inhomogeneous material properties due to non-uniform heating. Our mathematical analysis resolves the hitherto unexplained suppression of ET flow rate from experimental observation, wherein a subtle decrease of salt concentration is observable on top of the electrode gap of a maximum

temperature rise in the context of a standard electrokinetic pump. ET-based active control of ion current transport can be possibly used for a broad spectrum of applications ranging from seawater desalination, drug screening to biomolecule preconcentration.

Moreover, the delicate combinations of EO, ET, and NC are even more efficient to control the dynamic growth of DBL, by inducing more intense convective mixing. Simulation of ion current control with the improved physical understanding, which considers microscopic conservation laws, can provide new physical insights into the design of ET-based micro/nanofluidic devices having multiple functionalities. It is our belief that the current microscopic perspective for ET is about to advance interdisciplinary sciences on condensed matter, analytical chemistry, and electrokinetic phenomena.

This project is financially supported by the National Natural Science Foundation of China (No.11672095, No.11702035, No.11702075, No.71871027), Opening fund of State Key Laboratory of Nonlinear Mechanics, the Chang'an University Fundamental Research Funds for the Central Universities (No. 310832171008, No. 300102328201, No. 300102328501), Shaanxi kefa [2018] No. 9 key industrial innovation chain (group)-industrial field (No. 2018ZDCXL-GY-05-04, No. 2018ZDCXL-GY-05-07-02), Self-Planned Task (SKLRS201803B) of State Key Laboratory of Robotics, and System (HIT).

The authors have declared no conflict of interest.

5 References

- [1] Hu, G., Li, D., *Chem. Eng. Sci.* 2007, 62, 3443–3454.
- [2] Squires, T. M., Quake, S. R., *Rev. Mod. Phys.* 2005, 77, 977.
- [3] Ramos, A., Morgan, H., Green, N. G., Castellanos, A., *J. Phys. D: Appl. Phys.* 1998, 31, 2338.
- [4] Jarrod, S., Sinwook, P., Gilad, Y., *Phys. Rev. Lett.* 2013, 110, 204504.
- [5] Kunti, G., Bhattacharya, A., Chakraborty, S., *Int. J. Heat Mass Transfer* 2017, 109, 215–222.
- [6] Kunti, G., Bhattacharya, A., Chakraborty, S., *J. Non-Newtonian Fluid Mech.* 2017, 247, 123–131.
- [7] Chen, L., Lee, S., Choo, J., Lee, E. K., *J. Micromech. Microeng.* 2007, 18, 013001.
- [8] Chen, L., Ma, J., Guan, Y., *J. Chromatogr. A* 2004, 1028, 219–226.
- [9] Beni, G., Tenan, M., *J. Appl. Phys.* 1981, 52, 6011–6015.
- [10] Ramos, A., *Electrokinetics and electrohydrodynamics in microsystems*, Springer Science & Business Media, Wien, 2011.
- [11] Richter, A., Sandmaier, H., *IEEE Proc. Micro Electro Mech. Syst.* 1990, pp. 99–104.
- [12] Liu, W., Ren, Y., Shao, J., Jiang, H., Ding, Y., *J. Phys. D: Appl. Phys.* 2014, 47, 075501.
- [13] Iverson, B. D., Garimella, S. V., *J. Micromech. Microeng.* 2009, 19, 055015.
- [14] Gimsa, J., Eppmann, P., Prüger, B., *Biophys. J.* 1997, 73, 3309.
- [15] Melcher, J. R., Firebaugh, M. S., *Phys. Fluids* 1967, 10, 1178–1185.
- [16] Bazant, M. Z., Squires, T. M., *Phys. Rev. Lett.* 2004, 92, 066101.
- [17] Squires, T. M., Bazant, M. Z., *J. Fluid Mech.* 2004, 509, 217–252.
- [18] Ren, Y., Liu, W., Jia, Y., Tao, Y., Shao, J., Ding, Y., Jiang, H., *Lab Chip* 2015, 15, 2181–2191.
- [19] Liu, W., Shao, J., Jia, Y., Tao, Y., Ding, Y., Jiang, H., Ren, Y., *Soft matter* 2015, 11, 8105–8112.
- [20] Peng, C., Lazo, I., Shiyanovskii, S. V., Lavrentovich, O. D., *Phys. Rev. E: Stat. Nonlinear Soft Matter Phys.* 2014, 90, 051002.
- [21] Schnitzer, O., Yariv, E., *Phys. Rev. E: Stat. Nonlinear Soft Matter Phys.* 2012, 86, 061506.
- [22] Yossifon, G., Frankel, I., Miloh, T., *Phys. Fluids* 2007, 19, 217.
- [23] Yossifon, G., Frankel, I., Miloh, T., *Phys. Fluids* 2006, 18, 381.
- [24] Boymelgreen, A. M., Balli, T., Miloh, T., Yossifon, G., *Nat. Commun.* 2018, 9.
- [25] Jia, Y., Ren, Y., Hou, L., Liu, W., Jiang, T., Deng, X., Tao, Y., Jiang, H., *Lab Chip* 2018, 18, 1121–1129.
- [26] Jia, Y., Ren, Y., Hou, L., Liu, W., Deng, X., Jiang, H., *Small* 2017, 13, 1702188.
- [27] Hou, L., Ren, Y., Jia, Y., Deng, X., Liu, W., Feng, X., Jiang, H., *ACS Appl. Mater. Interfaces* 2017, 9, 12282–12289.
- [28] Jia, Y., Ren, Y., Liu, W., Hou, L., Tao, Y., Hu, Q., Jiang, H., *Lab Chip* 2016, 16, 4313–4318.
- [29] Boymelgreen, A., Yossifon, G., Miloh, T., *Langmuir* 2016, 32, 9540–9547.
- [30] Green, Y., Eshel, R., Park, S., Yossifon, G., *Nano Lett.* 2016, 16, 2744–2748.
- [31] Gimsa, J., Stubbe, M., Gimsa, U., *J. Electr. Bioimped.* 2014, 5, 74–91.
- [32] Yuan, Q., Yang, K., Wu, J., *Microfluid. Nanofluid.* 2014, 16, 167–178.
- [33] Lian, M., Islam, N., Wu, J., *IET Nanobiotechnol.* 2007, 1, 36–43.
- [34] Liu, W., Ren, Y., Tao, Y., Yao, B., Li, Y., *Electrophoresis* 2018, 39, 779–793.
- [35] Liu, W., Ren, Y., Tao, Y., Chen, X., Wu, Q., *Micromachines* 2017, 8, 327.
- [36] Li, Y., Ren, Y., Liu, W., Chen, X., Tao, Y., Jiang, H., *Electrophoresis* 2017, 38, 983–995.
- [37] Kunti, G., Bhattacharya, A., Chakraborty, S., *Phys. Fluids* 2018, 30, 062004.
- [38] Liu, W., Ren, Y., Tao, Y., Yao, B., Liu, N., Wu, Q., *Phys. Fluids* 2017, 29, 112001.
- [39] Li, Z., Liu, W., Gong, L., Zhu, Y., Gu, Y., Han, J., *Int. J. Appl. Mech.* 2017, 9, 1750107.
- [40] Yan, Y., Schiffbauer, J., Yossifon, G., Chang, H. C., *J. Chem. Phys.* 2015, 143, 80.
- [41] Mavrogianis, N., Desmond, M., Gagnon, Z. R., *Electrophoresis* 2015, 36, 1386–1395.
- [42] Ding, Z., Wong, T. N., *Phys. Rev. E: Stat. Nonlinear Soft Matter Phys.* 2014, 89, 033010.
- [43] García-Sánchez, P., Ferney, M., Ren, Y., Ramos, A., *Microfluid. Nanofluid.* 2012, 13, 441–449.
- [44] Ren, Y., Jiang, H., Yang, H., Ramos, A., García-Sánchez, P., *J. Electrostat.* 2009, 67, 372–376.

- [45] Jd, P., Jg, S., *APS Division of Fluid Dynamics Meeting* 2004, pp. 145–150.
- [46] Melcher, J. R., *Phys. Fluids* 1966, 9, 1548–1555.
- [47] Liu, W., Ren, Y., Tao, Y., Chen, X., Yao, B., Hui, M., Bai, L., *Phys. Fluids* 2017, 29, 112002.
- [48] Velev, O. D., Gangwal, S., Petsev, D. N., *Annu. Rep. Prog. Chem., Sect. C: Phys. Chem.* 2009, 105, 213–246.
- [49] Stubbe, M., Gimsa, J., *Colloids Surf. A* 2011, 376, 97–101.
- [50] Stubbe, M., Gyurova, A., Gimsa, J., *Electrophoresis* 2013, 34, 562–574.
- [51] Golak, K., Anandaroop, B., Suman, C., *Phys. Fluids* 2018, 30, 082005.
- [52] Kunti, G., Bhattacharya, A., Chakraborty, S., *Soft Matter* 2017, 13.
- [53] Kunti, G., Bhattacharya, A., Chakraborty, S., *Electrophoresis* 2017, 38, 1310–1317.
- [54] González, A., Ramos, A., Morgan, H., Green, N. G., Castellanos, A., *J. Fluid Mech.* 2006, 564, 415–433.
- [55] Loire, S., Kauffmann, P., Mezić, I., Meinhart, C., *J. Phys. D: Appl. Phys.* 2012, 45, 185301.
- [56] Wu, J., Lian, M., Yang, K., *Appl. Phys. Lett.* 2007, 90, 234103.
- [57] Park, S., Yossifon, G., *Nanoscale* 2018, 10, 11633–11641.
- [58] Leinweber, F. C., Eijkel, J. C. T., Bower, J. G., van den Berg, A., *Anal. Chem.* 2006, 78, 1425–1434.
- [59] Green, Y., Yossifon, G., *Phys. Rev. E: Stat. Nonlinear Soft Matter Phys.* 2015, 91, 063001.
- [60] Chang, H. C., Yossifon, G., Demekhin, E. A., *Annu. Rev. Fluid Mech.* 2012, 44, 401–426.
- [61] Haynes, W. M., *Financijska Teorija I Praksa* 2012, 126, 81–84.
- [62] Du, E., Manoochehri, S., *J. Appl. Phys.* 2008, 104, 2584.
- [63] Kunti, G., Dhar, J., Bhattacharya, A., Suman, C., *J. Appl. Phys.* 2018, 123, 244901.
- [64] Gonzalez, A., Ramos, A., García-Sánchez, P., Castellanos, A., *Phys. Rev. E: Stat. Nonlinear Soft Matter Phys.* 2010, 81, 016320.
- [65] Salari, A., Navi, M., Dalton, C., *Biomicrofluidics* 2015, 9, 014113.
- [66] Green, N. G., Ramos, A., Gonzalez, A., Castellanos, A., Morgan, H., *J. Electrostat.* 2001, 53, 71–87.
- [67] Zehavi, M., Boymelgreen, A., Yossifon, G., *Phys. Rev. Appl.* 2016, 5, 044013.